Dalton Transactions

ROYAL SOCIETY OF CHEMISTRY

PAPER

View Article Online
View Journal | View Issue

Check for updates

Cite this: *Dalton Trans.*, 2024, **53**, 12755

Tuning the dimensionality in chiral and racemic organic/tin hybrids with halides†

Louis Caussin,[a,b,c] Abdelaziz Jouaiti,[a] Daniel Chartrand,[d] W. G. Skene[b,c] and Sylvie Ferlay*[a]

Received 5th June 2024,
Accepted 1st July 2024

DOI: 10.1039/d4dt01645a

rsc.li/dalton

Chiral 1D tin iodides EBASnI$_3$ were synthesized while incorporating enantiomerically pure and racemic ethylbenzylammonium (EBA) cations between the 1D shared inorganic corners. The dimensionality was reduced to 0D when replacing iodine with bromine. In all the cases, the presence of hydrogen bonds was observed between the organic part and the inorganic part, while transfer of chirality was evidenced for the EBASnI$_3$ enantiomerically pure compounds.

Introduction

Hybrid organic–inorganic metal halide perovskites (HOIPs) are a family of crystalline semiconductors that display a large variety of dimensionalities.[1–4] The opto-electronic properties of HOIPs are compatible for their use in a wide range of applications, including photovoltaics,[2,5,6] light-emitting devices, and photodetectors.[7] Although HOIPs are intrinsically achiral, chirality can be induced by incorporating chiral organic molecules into the network.[8] The benefit of chirality is that it enhances the properties of HOIPs and it expands their uses to include nonlinear optical responses, ferroelectricity, emission- and spin-dependent transport, and circularly polarized light absorption with tuneable wavelength. These have opened new opportunities for chiroptics and chiroptoelectronic applications.[9] Since the original report of chiral HOIPs in 2006,[10] the field has advanced to include 2D lead-halide layered perovskites (Ruddlesden–Popper [RP] phases) with chiral aromatic ammonium as templating cations,[11–13] for example.

The development of chiral metal halides with functional properties has evolved according to two different approaches. On one hand, property enhancement has been pursued by decreasing the dimensionality of metal halide systems from one dimension (1D)[14,15] to zero order (0D).[16] On the other hand, commonly used lead[17] has been replaced with other metal ions such as Bi, In, Ge, As, Sb or Sn cations. The latter has only recently emerged as an interesting candidate to expand the number of metal halide compounds and further improve some properties. Indeed, 2D/3D tin perovskites have successfully been used in solar cells[18–23] and electronic devices.[24] The performance of solar cells can further be improved with mixed metals such as the combination of lead and tin.[25,26]

Despite the advantages of tin halides for property improvement, only a limited number of such derivatives have been reported. Examples are restricted to the use of methylbenzylammonium (MBA) monovalent cationic 2D tin(II) iodide perovskites,[27,28] (*R*-/*S*-MBA)$_2$Sn^{II}I$_4$, and their racemate (*rac*-MBA)$_2$Sn^{II}I$_4$. Their chlorinated counterparts[29] and mixed lead–tin phases have also been used in spin polarized charge transport (CPL) and solar cells.[30] Recently the first second-harmonic generation-active 1D tin(II)-based chiral hybrid perovskite has been reported.[31] In parallel, 0D tin(IV) chiral bromines have been prepared from β-methylphenethylamine (MPEA) cations and the [*R*/*S*/*rac*(MPEA)]$_2$Sn^{IV}Br$_6$ derivatives exhibited second-order nonlinear optical properties.[32] The band gap (E_g) of such systems can also be adjusted by replacing the cation. For example, it is possible to obtain a high E_g of 4.11 eV by incorporating the 3-hydroxyquinuclidinium cation (HQ) into the structure of chiral [*R*/*S*(HQ)]$_2$Sn^{IV}Cl$_6$.[33] Nonlinear optical properties can also be added using chlorinated or fluorinated chiral methylbenzyl ammonium cations as in [*R*/*S*/*rac*(XMBA)]$_2$Sn^{IV}Cl$_6$.[34]

Building upon chiral HOIPs and contributing to understanding the effect of halides on ordering and chirality on the optical properties, herein we report six new chiral tin halides. The low dimensionality tin halides evaluated are 1D (*R*-/*S*-/*rac*-EBA)-Sn^{II}I$_3$ and 0D (*R*-/*S*-/*rac*-EBA)$_2$-Sn^{IV}Br$_6$. To the best of our knowledge, 0D and 1D Sn structures have not been reported with the chiral ethylbenzylammonium cation (EBA; Fig. 1). As

[a]*CNRS, CMC UMR 7140, Université de Strasbourg, 4 rue Blaise Pascal, CS 90032, 67081 Cedex Strasbourg, France. E-mail: ferlay@unistra.fr*
[b]*Laboratoire de Caractérisation Photophysique des Matériaux Conjugués, Département de Chimie, Université de Montréal, CP 6128, succ. Centre-ville, Montréal, Québec, H3C 3J7, Canada*
[c]*Institut Courtois, Université de Montréal, Montréal, Québec, Canada*
[d]*Plateform de Rayons-X, Département de Chimie, Université de Montréal, CP 6128, succ. Centre-ville, Montréal, Québec, H3C 3J7, Canada*

†Electronic supplementary information (ESI) available: Bond distances and angles, shape analysis, PXRD data, UV visible data, and computed electronic band structures. CCDC 2358999–2359004. For ESI and crystallographic data in CIF or other electronic format see DOI: https://doi.org/10.1039/d4dt01645a

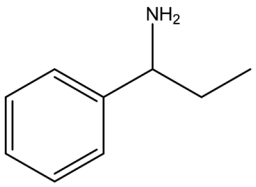

Fig. 1 Ethylbenzylamine (EBA) amine precursor used for preparing chiral tin halides.

such, we prepared (*R*-/*S*-/*rac*)-(EBA) derivatives to demonstrate that their dimensionality is underpinned by the nature of the halogen atom. The structural analyses concomitant with the solid-state and solution spectroscopic analyses are described and the transfer of chirality of EBA to tin iodine is confirmed.

Results and discussion

The series of compounds have been characterized from a structural point of view, their optical properties have been evaluated and their optical band gaps and electronic structures have also been calculated.

Synthesis and structure of 1D (*R*/*S*/*rac*-EBA)-$Sn^{II}I_3$

Colorless needle-like crystals of chiral *R*-/*S*-**EBA**-$Sn^{II}I_3$ and racemic 1D *rac*-**EBA**-$Sn^{II}I_3$ were synthesized under an inert atmosphere using a mixture of aqueous hydriodic acid (57%), EBA, SnO_2 and aqueous hypophosphorous acid (50%) according to a previously reported method (see the Experimental section).[27] Colorless crystals that were suitable for X-ray diffraction were formed after letting the solution sit for 1 day. The three compounds crystallized in an orthorhombic system. The isostructural (*R*/*S*-**EBA**)$_2Sn^{II}I_3$ compounds adopt a $P2_12_12_1$ non-centrosymmetric Sohncke space group, while *rac*-**EBA**-$Sn^{II}I_3$ is *Pnma* centrosymmetric (Table 1). It is interesting to note that the three compounds have consistent cell parameters and cell volumes. The asymmetric unit of the racemic and chiral compounds is based on one independent protonated EBA cation and one $Sn^{II}I_3^-$ anion belonging to the $(SnI_3)_n^{n-}$ infinite chain, running along the *a* axis. The crystal structure is based on cationic protonated monovalent cations and the anionic inorganic SnI_3^- chains formed by face-sharing metal–halide octahedra. The compounds are one-dimensional, being the first time such a chiral 1D tin halide has been observed. For the three compounds, the chains are separated by protonated amines (Fig. 2). In the racemic compound, the cationic unit is disordered. For (*R*/*S*-**EBA**)-$Sn^{II}I_3$ compounds, there is a helicoidal *M* and *P* chirality associated with the inorganic chains that are not superimposable, as shown in Fig. S1 (ESI†). This is an indication that there is transfer of chirality from the organic ligand to the inorganic part. The enantiomerically pure compounds present flack parameters in accordance with their chirality (0.102(2) and 0.03(3) for (*R*/*S*-**EBA**)-$Sn^{II}I_3$, respectively).

For the three reported compounds, the metal cations are in a distorted octahedral environment, as shown by both the angles and the distances reported in Table S1, ESI.† This is also in accordance with the shape analysis (*vide infra*). There are weak hydrogen bonds in the three compounds between the protonated amine and iodine from the $Sn^{II}I_3^-$ anions with d_{N-I} in the 3.5180(11)–3.8965(9) Å range (see Table S1 and Fig. S2 in the ESI†). There are also CHI contacts with d_{C-I} in the 3.6158(14)–3.9526(8) Å range.

Such $(MX_3^-)_n$ 1D chains separated by EBA cations have been observed with lead bromine analogues.[35] The reported structures have similar unit cell parameters. The (*S*)- or (*R*)-**EBA**-SnI_3 structures show a contraction of the *c* axis, due to the dilation of the *a* and *b* axes; since $(SnI_3^-)_n$ presents a larger size than $(PbBr_3^-)_n$ analogues, EBA can adopt a steeper packing angle.

Synthesis and structure of 0D (*R*/*S*/*rac*-EBA)$_2$-$Sn^{IV}Br_6$

Chiral (*R*/*S*-**EBA**)$_2$-$Sn^{IV}Br_6$ and racemic (*rac*-**EBA**)$_2$-$Sn^{IV}Br_6$ were also crystallized under the above-described conditions, and HI was replaced with concentrated hydrobromic acid (see the Experimental section). It is interesting to note that Sn^{2+} oxidizes to Sn^{4+} when using HBr, as previously observed.[36] The formation of stable and stereochemically inactive $Sn^{IV}Br_6^{2-}$ species leads, when combined with cations, to a different stoichiometries between the cations and the organic anions, and a 0D system is adopted.

Pale yellow crystals, suitable for X-ray diffraction, appear after 1 day of letting the solution sit. The three compounds crystallize in an orthorhombic system, a $P2_12_12_1$ non-centrosymmetric Sohncke space group for the chiral isostructural (*R*/*S*-**EBA**)$_2$-$Sn^{IV}Br_6$ compounds (Table 1). In contrast, (*rac*-**EBA**)$_2$-$Sn^{IV}Br_6$ crystallizes in the centrosymmetric *Pbca* space group. It is interesting to note that the three compounds present a similar cell volume. The asymmetric unit of the crystal structures of the isolated enantiomers contains two protonated EBA cations and one $Sn^{IV}Br_6^{2-}$ anion. Their racemate counterpart contains only one cation and one $Sn^{IV}Br_3^-$ anion, being a mirror image (Fig. 3). The enantiomerically pure compounds present flack parameters in accordance with their chirality (0.069(8) and 0.058(13) (*R*/*S*-**EBA**)$_2$-$Sn^{IV}Br_6$, respectively).

For the three compounds, the $Sn^{IV}Br_6^{2-}$ anions and EBA cations are independent. The metal cations are in a distorted octahedral environment with respect to both the angles and the distances reported in Table S1, ESI† (see also the SHAPE analysis below). The distances and angles are also in accordance with other salts containing the $Sn^{IV}Br_6^{2-}$ anion.[32,37] Some weak hydrogen bonds are present in the three compounds. These occur between the protonated amine and the bromine from the $Sn^{IV}Br_6^{2-}$ anions with d_{N-Br} in the 3.3985(6)–3.7629(5) Å range (see Table S1 and Fig. S3 in the ESI†). There are also CH···Br contacts with d_{C-Br} in the 3.5845(6)–3.7233(6) Å range.

Structural distortion analysis

The distortions around the $Sn^{2+/4+}$ cations in the 0 and 1D compounds were analyzed with the SHAPE program.[38,39] For 0D (*S*)- or (*R*)-**EBA**$_2$-$SnBr_6$ and (*rac*)-**EBA**$_2$-$SnBr_6$, the octahedral

Table 1 Crystallographic data for ((*R*)-**EBA**)$_2$-SnBr$_6$, ((*S*)-**EBA**)$_2$-SnBr$_6$, (*rac*-**EBA**)$_2$-SnBr$_6$, (*R*)-**EBA**-SnI$_3$, (*S*)-**EBA**-SnI$_3$ and *rac*-**EBA**-SnI$_3$ measured at 150 K

	((*R*)-**EBA**)$_2$-SnBr$_6$	((*S*)-**EBA**)$_2$-SnBr$_6$	(*rac*-**EBA**)$_2$-SnBr$_6$	(*R*)-**EBA**-SnI$_3$	(*S*)-**EBA**-SnI$_3$	(*rac*)-**EBA**-SnI$_3$
Formula	$SnBr_6$, $(C_9H_{14}N)_2$	$SnBr_6$, $(C_9H_{14}N)_2$	$SnBr_6$, $(C_9H_{14}N)_2$	(SnI_3, $(C_9H_{14}N)$)	(SnI_3, $(C_9H_{14}N)$)	SnI_3, $(C_9H_{14}N)$
Molecular weight (g mol^{-1})	870.57	870.57	870.57	1271.20	635.60	635.60
Crystal system	Orthorhombic	Orthorhombic	Orthorhombic	Orthorhombic	Orthorhombic	Orthorhombic
Space group	$P2_12_12_1$	$P2_12_12_1$	*Pbca*	$P2_12_12_1$	$P2_12_12_1$	*Pnma*
a (Å)	7.5715(3)	7.5756(3)	7.5056(4)	8.5559(2)	8.5537(4)	8.2467(3)
b (Å)	17.9623(7)	17.9704(6)	13.0933(8)	8.6602(2)	8.6479(3)	8.5854(3)
c (Å)	20.2642(9)	20.2660(7)	27.1689(16)	20.3328(6)	20.3305(9)	21.7734(8)
α (deg.)	90	90	90	90	90	90
β (deg.)	90	90	90	90	90	90
γ (deg.)	90	90	90	90	90	90
V (Å^3)	2756.0(2)	2758.94(17)	2670.0(3)	1506.58(7)	1503.88(11)	1541.58(10)
Z	4	4	4	2	4	4
Colour	Yellow	Yellow	Yellow	Colourless	Colourless	Colourless
Crystal dim. (mm^3)	0.140 × 0.08 × 0.08	0.060 × 0.03 × 0.03	0.120 × 0.110 × 0.060	0.086 × 0.030 × 0.030	0.086 × 0.030 × 0.030	0.060 × 0.045 × 0.030
$D_{calc.}$ (g cm^{-3})	2.098	2.096	2.166	2.802	2.807	2.739
F(000)	1640	1640	1640	1136	1136	1136
μ (mm^{-1})	11.843	11.830	12.225	42.125	42.201	41.308
Wavelength (Å)	1.34139	1.34139	1.34139	1.34139	1.34139	1.34139
Number of data meas.	6331	6939	2685	3432	3534	1874
Number of data with $I > 2\sigma(I)$	5787 [*R*(int) = 0.0274]	4884 [*R*(int) = 0.0481]	2198 [*R*(int) = 0.00371]	3399 [*R*(int) = 0.0276]	3175 [*R*(int) = 0.0370]	1631 [*R*(int) = 0.0364]
R (%)	R_1 = 0.0274, wR_2 = 0.0317	R_1 = 0.0481, wR_2 = 0.0966	R_1 = 0.0371, wR_2 = 0.0497	R_1 = 0.0276, wR_2 = 0.0279	R_1 = 0.0370, wR_2 = 0.0421	R_1 = 0.0364, wR_2 = 0.0433
R_w (%)	R_1 = 0.0633, wR_2 = 0.0652	R_1 = 0.1124, wR_2 = 0.1242	R_1 = 0.0840, wR_2 = 0.0889	R_1 = 0.0683, wR_2 = 0.0684	R_1 = 0.0868, wR_2 = 0.0893	R_1 = 0.1198, wR_2 = 0.1246
GOF	1.042	0.966	1.076	1.109	0.998	1.108
Flack	0.069(8)	0.058(13)	—	0.10(2)	0.03(3)	—
Largest peak in the final difference (e Å^{-3})	0.866 and −0.668	1.184 and −0.518	0.900 and −0.666	1.328 and −1.696	1.483and −0.648	1.267 and −0.830

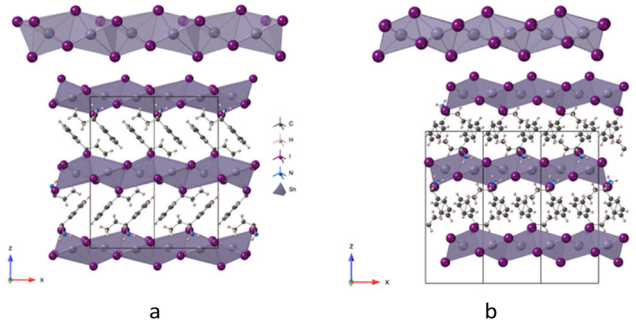

Fig. 2 Representative structures of (a) (*S*)- or (*R*)-**EBA**-SnI_3 and (b) (*rac*)-**EBA**-SnI_3: projection in the *xOz* planes. Schematic polyhedral representation of one SnI_3^- anionic inorganic chain along the *a* axis. The organic cations are disordered in (*rac*)-**EBA**-SnI_3. For bond distances, see the text and the ESI.†

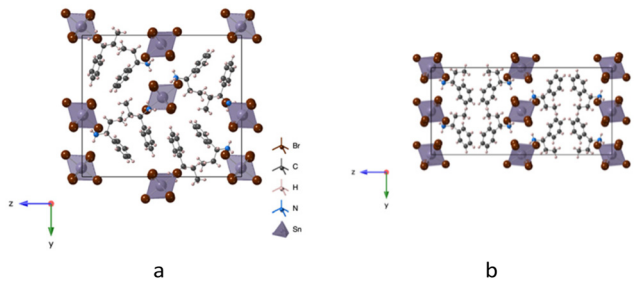

Fig. 3 Representative structures of (a) ((*S*)- or (*R*)-**EBA**)$_2$-$SnBr_6$ and (b) ((*rac*)-**EBA**)$_2$-$SnBr_6$: projection in the *yOz* planes. For bond distances, see the text and the ESI.†

distortion was determined using a $SnBr_6^{2-}$ O_h model with CShM (continuous shape measurements) with values varying between 19.056 and 19.324 (see the ESI†). The octahedral distortion determined using a SnI_6 O_h model is lower for 1D (*S*)- and (*R*)-**EBA**-SnI_3 along with (*rac*)-**EBA**-SnI_3 , varying around 17.12. These constraints are owing to distorted 1D $(SnI_3^-)_n$ units.

For all the compounds, the high values are in accordance with a strongly distorted environment around the metal, deviating from the octahedral model.

PXRD of the compounds

The polycrystalline powders were further analysed by PXRD. The PXRD patterns obtained for the polycrystalline samples are consistent with their calculated diagrams (Fig. 4). This confirms that the microcrystalline powders of (*S*)- or (*R*)-**EBA**$_2$-$SnBr_6$ and (*rac*)-**EBA**$_2$-$SnBr_6$ don't contain trace of impurities and other crystalline phases. The 0D compounds are stable in air in the solid state. They are also partially soluble in DMF.

This contrasts with the behaviour of compounds (*S*)- and (*R*)-**EBA**-SnI_3 and also (*rac*)-**EBA**-SnI_3 whose PXRD patterns indicate that the compounds decompose when exposed to air (see Fig. S4 in the ESI†). These compounds are highly soluble in DMF.

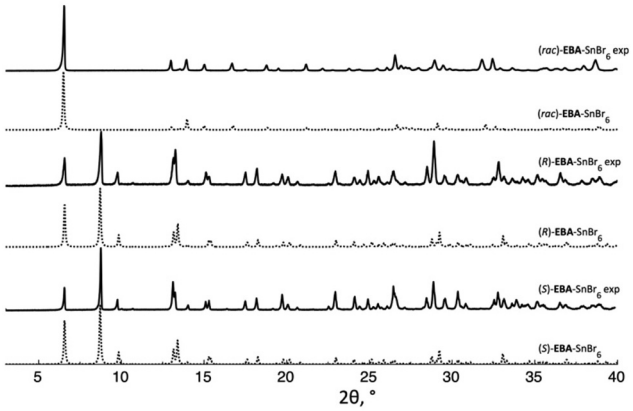

Fig. 4 Comparison of the simulated (dotted line) and experimental (solid line) powder X-ray diffraction (PXRD) diagrams for ((*S*)- or (*R*)-**EBA**)$_2$-$SnBr_6$ and ((*rac*)-**EBA**)$_2$-$SnBr_6$.

Preparation of films and optical characterization

Films are formed for the study of the optical properties. Homogeneous and contiguous films of all the compounds are obtained by drop-casting a DMF solution of the crystals (see the Experimental part for more details).

The linear absorption of the compounds is one of the most important properties. Indeed, the efficiency of photovoltaic devices is directly linked to the number of photons that can be absorbed by the active layer. This optical property is also desired for other optoelectronic applications. The linear absorption was measured in DMF for both series of compounds (Fig. S5†) and as thin polycrystalline films (Fig. 5). The absorption of the solution was measured between 300 and 800 nm. The freshly prepared compounds all display an absorption in the UV region that tails off by 350 nm ($C = 5 \times 10^{-4}$ M). Similarly, thin films of ((*S*)- and (*R*)-**EBA**)$_2$-$SnBr_6$ and ((*rac*)-**EBA**)$_2$-$SnBr_6$ absorbed below 350 nm. A new absorption occurs at 370 nm concomitant with an extension of the absorption out to 700 nm after the oxidation of (*S*)- or (*R*)-**EBA**-SnI_3 and (*rac*)-**EBA**-SnI_3. This aside, the linear absorption spectra of the *R*-, *S*-, and *rac*-films are consistent. It is also interesting to note that none of the studied compounds were emissive under irradiation in the 350 nm region, whether it be in solution or films.

Transmission circular dichroism (CD) measurements were also performed for both series of the compounds as thin films (Fig. 6). The CD peaks appear at the same wavelength: 370 nm for (*S*)- and (*R*)-**EBA**-SnI_3; 310 nm for ((*S*)- and (*R*)-**EBA**)$_2$-$SnBr_6$ with the enantiomers absorbing with opposite signs, in accordance with the absorption properties. The chirality was further confirmed by the racemate that exhibited no CD spectrum.

Electronic band structures

First-principles calculations using DFT were used to examine the electronic structure of the 0D and 1D chiral tin halides. Given that the X-ray data are of high quality and they represent

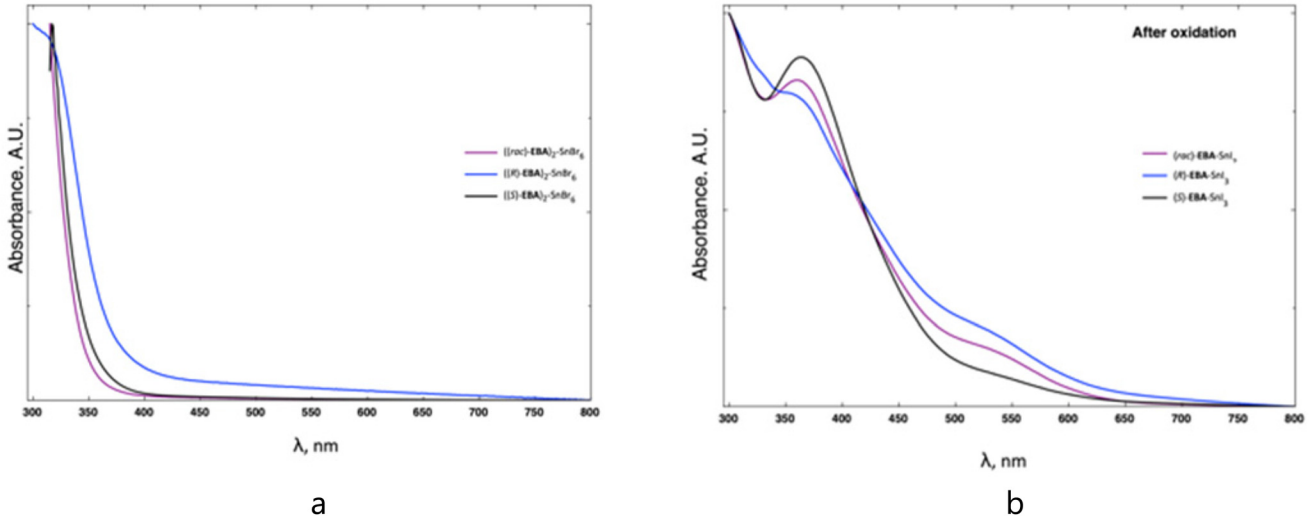

Fig. 5 Absorption spectra of the films of the chiral tin halide: (a) 0D ((*S*)- and (*R*)-**EBA**)$_2$-SnBr$_6$ and ((*rac*)-**EBA**)$_2$-SnBr$_6$; (b) 1D series (*S*)- and (*R*)-**EBA**-SnI$_3$ and (*rac*)-**EBA**-SnI$_3$ after their oxidation in air.

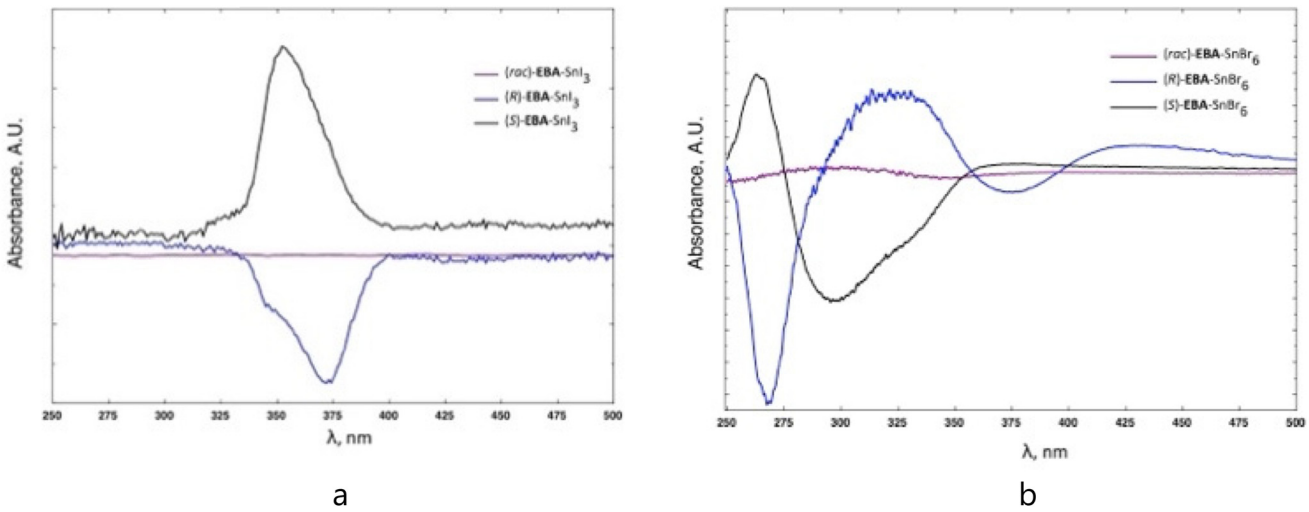

Fig. 6 Circular dichroism (CD) spectra of the films of the chiral tin halide: (a) 0D ((*S*)- and (*R*)-**EBA**)$_2$-SnBr$_6$ and ((*rac*)-**EBA**)$_2$-SnBr$_6$; (b) 1D series (*S*)- or (*R*)-**EBA**-SnI$_3$ and (*rac*)-**EBA**-SnI$_3$.

the true solid-state arrangement of the atoms, these data were used for constructing a periodic array for the calculations. This was complemented by using the unit cell and its dimensions for the given tin halide to build the constitutional unit for upscaling the crystal to the bulk periodic array. The disorder of the crystal structure of (*rac*)-**EBA**-SnI$_3$ precludes its calculation. Although absolute values cannot be accurately calculated owing to systematic errors, these are consistent for each calculation. As a result, the data can be compared between calculations and trends, both reliably and accurately derived. This assumes that identical calculation methods are applied to the ensemble of study.

The salient feature of the band diagram that is common to both series of the tin halides is the non-metallic character. This is based on the noncontiguous valence and conductive bands across the Fermi level. Indeed, the clear disconnect between the two bands corresponds to a band gap (Fig. 7 and Fig. S6–S10). Consistent with the crystallographic data, the differences in the band diagrams are contingent on the ordering of the periodic array. The energy gap of the tin bromides is smaller by *ca.* 0.5 eV than their iodide counterparts. The p shell contributes predominately to the valence band for the tin halides. This orbital is split into corresponding p-1/2 and p-3/2 levels owing to spin–orbit coupling according to the density of states. The conductance bands of the iodide are also diffuse, consisting principally of the p-shell. The d-3/2 shell also contributes, albeit in a minor amount. This contrasts with the tin bromides whose conductance band is more diffuse with con-

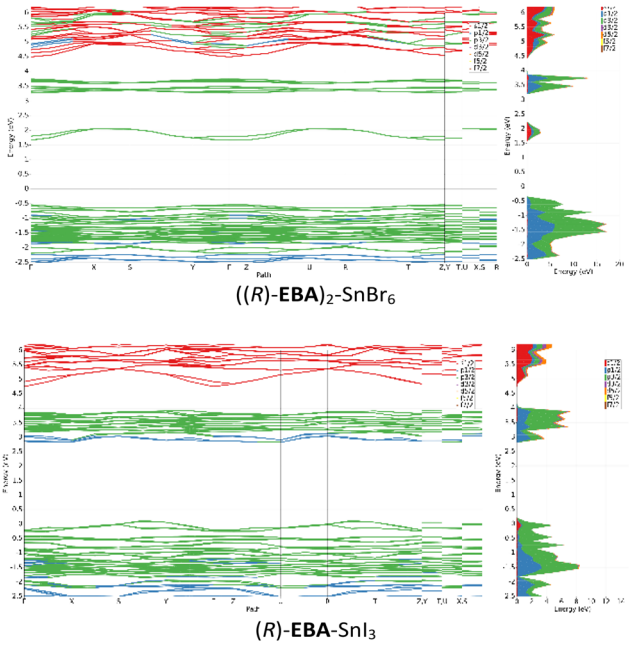

Fig. 7 Calclated electronic band structures of 0D ((*R*)-**EBA**)$_2$-SnBr$_6$ and 1D (*R*)-EBA-SnI$_3$. The contributions of electronic states to the bands are identified for Sn (red), I or Br (green), and organic-derived states (blue).

tributions from the s and p shells. There is also a small contribution from the d-5/2 shell. The bands are more diffuse for **EBA**$_2$-SnBr$_6$ and less diffuse for **EBA**-SnI$_3$. No difference between the enantiomerically pure compounds is found either for the band diagrams or the density of states other than the lower energy gap. This corroborates the experimental data that chirality does not affect the properties other than the circular dichroism.

Experimental

Synthetic procedures

All chemicals and reagents (starting amine) were of analytical grade and used as received from commercial sources (Sigma-Aldrich).

Crystals of (*S*)- or (*R*)-EBA-SnI$_3$ and (*rac*)-EBA-SnI$_3$

The synthesis of 1D crystals was performed according to previous reports.[27] The crystals were obtained in a nitrogen-saturated glovebox to prevent the oxidation of iodine and tin(II). SnO_2 was ground into a thin powder before the synthesis to increase its solubility. Grounded SnO_2 (140 mg), *R*-,*S*-,*rac*-**EBA** (200 μL), HI (6 mL), and H_3PO_2 (0.5 mL) were loaded into a round bottom flask. The mixture was then heated and stirred at 120 °C for roughly 8 h until SnO_2 was completely dissolved in a glovebox. The yellow clear solution was then left to slowly cool to room temperature. After 12 h, the resulting yellow needle-shaped crystals were filtered and were dried in the glovebox (yield ~65%).

Crystals of ((*S*)- or (*R*)-EBA)$_2$-SnBr$_6$ and ((*rac*)-EBA)$_2$-SnBr$_6$

The same procedure as described above was used, starting from a 2 : 1 molar ratio of *R*-,*S*-,*rac*-**EBA** and SnO_2 dissolved in HBr (6 mL). After 12 h, the yellow needle-shaped crystals that formed were filtered. They were then dried in the glovebox (yield ~65%).

Thin film preparation

Thin films of all compounds were prepared on square quartz/ITO substrates. First, the substrates were washed by ultrasonication in Hellmanex cleaning solution for 20 min. They were then treated in an ozone chamber for 30 min. Next, the given compound (20 mg) was weighed and dissolved in *N*,*N*-dimethylformamide (DMF; 1 mL). An aliquot (200 μL) of the solution was then drop-casted on a quartz slide (1.8 cm × 1.8 cm), followed by thermal annealing at 120 °C for 10 min to afford a uniform thin film. Similar steps were performed before for (*S*)- or (*R*)-**EBA**-SnI$_3$ and (*rac*)-**EBA**-SnI$_3$ and thermal annealing was performed in a glovebox. After thermal annealing, a second quartz substrate was placed over the film. The sandwich was sealed with epoxy to prevent the diffusion of oxygen and subsequent oxidation of the compounds.

Crystallography

X-ray data collection. Single-crystal X-ray diffraction (SXRD) data were collected at 150 K using an Oxford Cryostream 700 low-temperature device on a Bruker Venture Kappa-geometry diffractometer equipped with a gallium liquid-metal-jet source (Ga Kα radiation), a Photon III CMOS detector, and Helios MX mirror optics. Structures were solved using SHELXT 2018/2 and refined by full matrix least-squares on F^2 using SHELXL-2018/3. Hydrogen atoms were introduced either at calculated positions (riding model) or refined for H atoms belonging to H donor atoms (N, O) when data quality permits it. CCDC: (*S*)-**EBA**-SnI$_3$ (2359003), (*R*)-**EBA**-SnI$_3$ (2359002), (*rac*)-**EBA**-SnI$_3$ (2359004), ((*S*)-**EBA**)$_2$-SnBr$_6$ (2359000), ((*R*)-**EBA**)$_2$-SnBr$_6$ (2358999) and ((*rac*)-**EBA**)$_2$-SnBr$_6$ (2359001).†

Powder diffraction (PXRD) studies. Powder X-ray diffraction (PXRD) patterns were obtained in 30 minute scans with a range of $3° \leq 2\theta \leq 40°$ using a Malvern Panalytical Empyrean diffractometer 3 instrument equipped with a PIXcel3D detector, an Icore and Dcore optics set with automatic slits set at a 10 mm irradiated length, and a Cu Kα radiation source in Bragg Brentano (θ–θ) geometry.

Materials and methods

Structural deviation calculations. Structural deviation calculations for obtaining the CShM (Continuous Shape Measures) values were performed with the SHAPE program.[38] The computational details for the general polyhedral approach are found in the literature.[39]

Absorbance. Absorption spectra were recorded in solution at room temperature with an Agilent Cary 5000 spectrometer. Solutions of (*S*)- and (*R*)-**EBA**-SnI$_3$ and (*rac*)-**EBA**-SnI$_3$ were prepared in a glovebox with deoxygenated solvents. The spectro-

scopic cuvette was sealed to prevent the diffusion of oxygen. The absorption spectra were recorded using the sealed cuvette. The absorption spectra of the drop-casted thin films were also recorded at room temperature. Emission spectra were recorded using an Edinburgh Instruments FLSP-920 with the solutions deaerated and sealed in four window cuvettes. Similarly, the emission of the thin films was measured at 45° to the incident beam and detector.

Circular dichroism. Circular dichroism spectra of the drop-cast thin films were recorded in triplicate using a Jasco J-710 spectropolarimeter in the 250–500 nm range at a scan rate of 50 nm min^{-1}.

First-principles calculations. The single point energy for the periodic structures and the density of states were calculated with the BAND program[40] in AMS.[41] The X-ray crystallographic data were used for the calculations of the geometry and the periodic structure. The triple-zeta with two polarization functions (TZ2P) was used with a small frozen core as a compromise between the computer time and the accurate representation. The PBEsol[42,43] generalized gradient approximation density functional was used with the spin–orbit coupling relativity to calculate the single point energy. A normal numerical quality was used. The path through the Brillouin zone was generated automatically, corresponding to 12 paths through the orthorhombic structure: *G–X–S–Y–G–Z–U–R–T–Z|Y–T|U–X|S–R*. The corresponding *K*-points in fractional coordinates are: *G* (0.0, 0.0, 0.0); *R* (0.5, 0.5, 0.5); *S* (0.5, 0.5, 0.0); *T* (0.0, 0.5, 0.5); *U* (0.5, 0.0, 0.5); *X* (0.5, 0.0, 0.0); *Y* (0.0, 0.5, 0.0); and *Z* (0.0, 0.0, 0.5).

Conclusions

A series of chiral 1D $(SnI_3^-)_n$ tin iodides were synthesized by incorporating enantiomerically pure **EBA** cations between the 1D shared inorganic corners. In contrast, the dimensionality was reduced to 0D when replacing iodine with bromine in the edge-shared structures. The chiral organic cations distort the inorganic lattice by asymmetric hydrogen bonds and they transfer their chirality to the 1D inorganic arrays. Both series of tin halides crystallise in a chiral space group ($P2_12_12_1$), while their racemic counterparts crystallize in achiral space groups. The transfer of chirality of the EBA cation to the tin halides is confirmed by circularly polarized absorption in the 300–500 nm wavelength range of the inorganic Sn–X sublattice. The calculated band gap is in accordance with what have been determined with absorption measurements. This provides new examples for 1D and 0D tin halide-based compounds, presenting interesting absorption properties.

Author contributions

L. C.: formal analysis, investigation, and reviewing. A. J.: formal analysis and investigation. D. C.: formal analysis, investigation and reviewing. W. G. S.: formal analysis, conceptualization, supervision, writing and reviewing. S. F.: formal analysis, investigation, supervision, writing, reviewing and conceptualization.

Data availability

CCDC: (*S*)-**EBA**-SnI_3 (2359003), (*R*)-**EBA**-SnI_3 (2359002), (*rac*)-**EBA**-SnI_3 (2359004), ((*S*)-**EBA**)$_2$-$SnBr_6$ (2359000), ((*R*)-**EBA**)$_2$-$SnBr_6$ (2358999) and ((*rac*)-**EBA**)$_2$-$SnBr_6$ (2359001).†

Conflicts of interest

There are no conflicts to declare.

Acknowledgements

The Natural Sciences and Engineering Council Canada (NSERC) is thanked for providing an Alliance Catalyst grant that sustained this collaborative work. The Canada Foundation for Innovation is also thanked for providing various equipment and infrastructure funding that enabled the work. L. C. thanks both MITACS Globalink and the Université de Montréal for scholarships. Prof. L. Cuccia is greatly thanked for providing access for circular dichroism measurements. C. Amoah is thanked for his assistance with preliminary XRD analysis. The Digital Research Alliance of Canada (alliancecan.ca (**https://alliancecan.ca/**)) and its regional partner, Compute Ontario, are acknowledged for providing access to both computing resources and software. The Quebec Center for Advanced Materials is acknowledged for providing access to resources that enabled this work. The SCM support team is also thanked for providing insights for successful calculations. Financial support from the University of Strasbourg and the CNRS is acknowledged.

Notes and references

1 D. A. Egger, A. M. Rappe and L. Kronik, Hybrid Organic-Inorganic Perovskites on the Move, *Acc. Chem. Res.*, 2016, **49**, 573–581.
2 W. Li, Z. Wang, F. Deschler, S. Gao, R. H. Friend and A. K. Cheetham, Chemically diverse and multifunctional hybrid organic-inorganic perovskites, *Nat. Rev. Mater.*, 2017, **2**, 16099.
3 P. Gao, A. R. Bin Mohd Yusoff and M. K. Nazeeruddin, Dimensionality engineering of hybrid halide perovskite light absorbers, *Nat. Commun.*, 2018, **9**, 5028.
4 C. Katan, N. Mercier and J. Even, Quantum and Dielectric Confinement Effects in Lower-Dimensional Hybrid Perovskite Semiconductors, *Chem. Rev.*, 2019, **119**, 3140–3192.
5 J.-P. Correa-Baena, M. Saliba, T. Buonassisi, M. Grätzel, A. Abate, W. Tress and A. Hagfeldt, Promises and challenges of perovskite solar cells, *Science*, 2017, **358**, 739–744.

6 N. J. Jeon, J. H. Noh, W. S. Yang, Y. C. Kim, S. Ryu, J. Seo and S. I. Seok, Compositional Engineering of Perovskite Materials for High-Performance Solar Cells, *Nature*, 2015, **517**, 476–480.
7 Y. Fu, H. Zhu, J. Chen, M. P. Hautzinger, X.-Y. Zhu and S. Jin, Metal halide perovskite nanostructures for optoelectronic applications and the study of physical properties, *Nat. Rev. Mater.*, 2019, **4**, 169–188.
8 G. Long, R. Sabatini, M. I. Saidaminov, G. Lakhwani, A. Rasmita, X. Liu, E. H. Sargent and W. Gao, Chiral-perovskite optoelectronics, *Nat. Rev. Mater.*, 2020, **5**, 423–439.
9 J. Ma, H. Wang and D. Li, Recent Progress of Chiral Perovskites: Materials, Synthesis, and Properties, *Adv. Mater.*, 2021, **33**, 2008785.
10 D. G. Billing and A. Lemmerer, Synthesis and crystal structures of inorganic-organic hybrids incorporating an aromatic amine with a chiral functional group, *CrystEngComm*, 2006, **8**, 686–695.
11 Y. Dong, Y. Zhang, X. Li, Y. Feng, H. Zhang and J. Xu, Chiral Perovskites: Promising Materials toward Next-Generation Optoelectronics, *Small*, 2019, **15**, 1902237.
12 J. Ahn, S. Ma, J.-Y. Kim, J. Kyhm, W. Yang, J. A. Lim, N. A. Kotov and J. Moon, Chiral 2D Organic Inorganic Hybrid Perovskite with Circular Dichroism Tunable Over Wide Wavelength Range, *J. Am. Chem. Soc.*, 2020, **142**, 4206–4212.
13 X. Wang, Y. Wang, W. Gao, L. Song, C. Ran, Y. Chen and W. Huang, Polarization-Sensitive Halide Perovskites for Polarized Luminescence and Detection: Recent Advances and Perspectives, *Adv. Mater.*, 2021, **33**, 2003615.
14 T. Qiu, Y. Hu, F. Xu, Z. Yan, F. Bai, G. Jia and S. Zhang, Recent advances in one-dimensional halide perovskites for optoele,ctronic applications, *Nanoscale*, 2018, **10**, 20963–20989.
15 K. Hong, Q. Van Le, S. Y. Kim and H. W. Jang, Low-dimensional halide perovskites: review and issues, *J. Mater. Chem. C*, 2018, **6**, 2189–2209.
16 S. Sun, M. Lu, X. Gao, Z. Shi, X. Bai, W. W. Yu and Y. Zhang, 0D Perovskites: Unique Properties, Synthesis, and Their Applications, *Adv. Sci.*, 2021, **8**, 2102689.
17 Z. Shi, J. Guo, Y. Chen, Q. Li, Y. Pan, H. Zhang, Y. Xia and W. Huang, Lead-Free Organic-Inorganic Hybrid Perovskites for Photovoltaic Applications: Recent Advances and Perspectives, *Adv. Mater.*, 2017, **29**, 1605005.
18 J. Cao and F. Yan, Recent progress in tin-based perovskite solar cells, *Energy Environ. Sci.*, 2021, **14**, 1286–1325.
19 A. Abate, Stable Tin-Based Perovskite Solar Cells, *ACS Energy Lett.*, 2023, **8**, 1896–1899.
20 J. Zhao, Z. Zhang, G. Li, M. H. Aldamasy, M. Li and A. Abate, Dimensional Tuning in Lead-Free Tin Halide Perovskite for Solar Cells, *Adv. Energy Mater.*, 2023, **13**, 2204233.
21 X. Chang, G. Yang, J.-X. Zhong, Y. Tan and W.-Q. Wu, New Pathways toward Sustainable Sn-Related Perovskite Solar Cells, *Adv. Energy Sustainability Res.*, 2023, **4**, 2200175.
22 T. J. Macdonald, L. Lanzetta, X. Liang, D. Ding and S. A. Haque, Engineering Stable Lead-Free Tin Halide Perovskite Solar Cells: Lessons from Materials Chemistry, *Adv. Mater.*, 2023, **35**, 2206684.
23 S. Hu, J. A. Smith, H. J. Snaith and A. Wakamiya, Prospects for Tin-Containing Halide Perovskite Photovoltaics, *Precis. Chem.*, 2023, **1**, 69–82.
24 T. H. Chowdhury, Y. Reo, A. R. Bin Mohd Yusoff and Y.-Y. Noh, Sn-Based Perovskite Halides for Electronic Devices, *Adv. Sci.*, 2022, **9**, 2203749.
25 J. Seo, T. Song, S. Rasool, S. Park and J. Y. Kim, An Overview of Lead, Tin, and Mixed Tin–Lead-Based ABI_3 Perovskite Solar Cells, *Adv. Energy Sustainability Res.*, 2023, **4**, 2200160.
26 A. Yadegarifard, H. Leea, H.-J. Seok, I. Kim, B.-K. Ju, H.-K. Kim and D.-K. Lee, FA/Cs-based mixed Pb–Sn perovskite solar cells: A review of recent advances in stability and efficiency, *Nano Energy*, 2023, **112**, 108481.
27 H. Lu, C. Xiao, R. Song, T. Li, A. E. Maughan, A. Levin, R. Brunecky, J. J. Berry, D. B. Mitzi, V. Blum and M. C. Beard, Highly Distorted Chiral Two-Dimensional Tin Iodide Perovskites for Spin Polarized Charge Transport, *J. Am. Chem. Soc.*, 2020, **142**, 13030–13040.
28 W. Gao, H. Dong, N. Sun, L. Chao, W. Hui, Q. Wei, H. Li, Y. Xia, X. Gao, G. Xing, Z. Wu, L. Song, P. Müller-Buschbaum, C. Ran and Y. Chen, Chiral cation promoted interfacial charge extraction for efficient tin-based perovskite solar cells, *J. Energy Chem.*, 2022, **68**, 789–796.
29 C. Coccia, M. Morana, A. Mahata, W. Kaiser, M. Moroni, B. Albini, P. Galinetto, C. Milanese, A. Porta, E. Mosconi, F. De Angelis and L. Malavasi, Ligand-Induced Chirality in Novel 2D Tin Iodide Perovskite Cl-MBA_2SnI_4, *ChemRxiv*, 2023, preprint, DOI: 10.26434/chemrxiv-2023-kq7t5.
30 B. Yao, Q. Wei, Y. Yang, W. Zhou, X. Jiang, H. Wang, M. Ma, D. Yu, Y. Yang and Z. Ning, Symmetry-Broken 2D Lead–Tin Mixed Chiral Perovskite for High Asymmetry Factor Circularly Polarized Light Detection, *Nano Lett.*, 2023, **23**, 1938–1945.
31 K. Tao, Q. Li and Q. Yan, 1D Tin(II)-Based Chiral Hybrid Perovskite Single Crystals with Extremely Distorted Inorganic Chains for Second Harmonic Generation, *Adv. Opt. Mater.*, 2024, 2400018.
32 L. Zhao, X. Han, Y. Zheng, M.-H. Yu and J. Xu, Tin-Based Chiral Perovskites with Second-Order Nonlinear Optical Properties, *Adv. Photonics Res.*, 2021, **2**, 2100056.
33 H. Peng, Q. Liu, Y. Liu, Y. Lu and W. Liao, A chiral lead-free tin(IV)-based halide organic-inorganic semiconductor with dielectric switching and phase transition, *Chin. Chem. Lett.*, 2023, **34**, 107980.
34 X. Han, P. Cheng, R. Shi, Y. Zheng, S. Qi, J. Xu and X.-H. Bu, Linear optical afterglow and nonlinear optical harmonic generation from chiral tin(IV) halides: the role of lattice distortions, *Mater. Horiz.*, 2023, **10**, 1005–1011.
35 A. Jouaiti, N. Gruber, G. Delport, G. Trippé-Allard, J.-F. Guillemoles, E. Deleporte, S. Ferlay and D. Garrot, Using chiral ammonium cations to modulate the structure

of 1D hybrid lead bromide perovskites for linearly polarized broadband light emission at room temperature, *J. Mater. Chem. C*, 2022, **10**, 12436–12443.

36 G. Song, M. Li, Y. Yang, F. Liang, Q. Huang, X. Liu, P. Gong, Z. Xia and Z. Lin, Lead-Free Tin(IV)-Based Organic–Inorganic Metal Halide Hybrids with Excellent Stability and Blue-Broadband Emission, *Phys. Chem. Lett.*, 2020, **11**(5), 1808–1813.

37 X.-N. Hua, J.-X. Gao, T. Zhang, X.-G. Chen, D.-S. Sun, Y.-Z. Zhang and W.-Q. Liao, Switchable Dielectric Phase Transition with Drastic Symmetry Breaking in a Sn(IV)-Based Perovskite-Type Halide Semiconductor, *J. Phys. Chem. C*, 2019, **123**, 21161–21166.

38 M. Llunell, D. Casanova, J. Girera, P. Alemany and S. Alvarez, *SHAPE, version 2.1*, Universitat de Barcelona, Barcelona, Spain.

39 S. Alvarez, P. Alemany, D. Casanova, J. Cirera, M. Llunell and D. Avnir, Shape maps and polyhedral interconversion paths in transition metal chemistry, *Coord. Chem. Rev.*, 2005, **249**, 1693–1708.

40 G. te Velde and E. J. Baerends, Precise density-functional method for periodic structures, *Phys. Rev. B: Condens. Matter Mater. Phys.*, 1991, **44**, 7888.

41 P. H. T. Philipsen, G. te Velde, E. J. Baerends, J. A. Berger, P. L. de Boeij, M. Franchini, J. A. Groeneveld, E. S. Kadantsev, R. Klooster, F. Kootstra, M. C. W. M. Pols, P. Romaniello, M. Raupach, D. G. Skachkov, J. G. Snijders, C. J. O. Verzijl, J. A. Celis Gil, J. M. Thijssen, G. Wiesenekker, C. A. Peeples, G. Schreckenbach and T. Ziegler, *AMS 2023.102 r113752*, SCM, Theoretical Chemistry, Vrije Universiteit, Amsterdam, The Netherlands, **https://www.scm.com**.

42 J. P. Perdew, A. Ruzsinszky, G. I. Csonka, O. A. Vydrov, G. E. Scuseria, L. A. Constantin, X. Zhou and K. Burke, Restoring the Density-Gradient Expansion for Exchange in Solids and Surfaces, *Phys. Rev. Lett.*, 2008, **100**, 136406.

43 J. P. Perdew, A. Ruzsinszky, G. I. Csonka, O. A. Vydrov, G. E. Scuseria, L. A. Constantin, X. Zhou and K. Burke, Erratum: Restoring the Density-Gradient Expansion for Exchange in Solids and Surfaces, *Phys. Rev. Lett.*, 2009, **102**, 039902.